ARL-TR-7604 ● FEB 2016

US Army Research Laboratory

Utilizing the Power of Nanostructures to Their Fullest Capability in Energetic Formulations

by N Scott Weingarten, Jennifer L Gottfried, Iskander G Batyrev, Eric S Collins, and Michael R Zachariah

NOTICES

Disclaimers

The findings in this report are not to be construed as an official Department of the Army position unless so designated by other authorized documents.

Citation of manufacturer's or trade names does not constitute an official endorsement or approval of the use thereof.

Destroy this report when it is no longer needed. Do not return it to the originator.

ARL-TR-7604 ● FEB 2016

US Army Research Laboratory

Utilizing the Power of Nanostructures to Their Fullest Capability in Energetic Formulations

by N Scott Weingarten, Jennifer L Gottfried, Iskander G Batyrev, and Eric S Collins
Weapons and Materials Research Directorate, ARL

Michael R Zachariah
University of Maryland, College Park, MD

REPORT DOCUMENTATION PAGE

Form Approved
OMB No. 0704-0188

1. REPORT DATE *(DD-MM-YYYY)*	2. REPORT TYPE	3. DATES COVERED (From - To)
February 2016	Director's Research Initiative (DRI)	1 October 2012–30 September 2015

4. TITLE AND SUBTITLE
Utilizing the Power of Nanostructures to Their Fullest Capability in Energetic Formulations

5a. CONTRACT NUMBER

5b. GRANT NUMBER

5c. PROGRAM ELEMENT NUMBER

6. AUTHOR(S)
N Scott Weingarten, Jennifer L Gottfried, Iskander G Batyrev, Eric S Collins, Michael R Zachariah

5d. PROJECT NUMBER
DRI-13-WMR-008

5e. TASK NUMBER

5f. WORK UNIT NUMBER

7. PERFORMING ORGANIZATION NAME(S) AND ADDRESS(ES)
US Army Research Laboratory
ATTN: RDRL-WML-B
Aberdeen Proving Ground, MD 21005-5069

8. PERFORMING ORGANIZATION REPORT NUMBER
ARL-TR-7604

9. SPONSORING/MONITORING AGENCY NAME(S) AND ADDRESS(ES)

10. SPONSOR/MONITOR'S ACRONYM(S)

11. SPONSOR/MONITOR'S REPORT NUMBER(S)

12. DISTRIBUTION/AVAILABILITY STATEMENT
Approved for public release; distribution is unlimited.

13. SUPPLEMENTARY NOTES

14. ABSTRACT
The significantly enhanced energy release expected from energetic formulations containing nanostructured aluminum (Al) has never been realized due to sintering of the nano-Al just prior to the energy release step. This precludes achieving the faster energy release, more efficient combustion, and controllable explosive performance consistent with the introduction of nanostructured metallics to energetic formulations. This DRI project used complementary experimentation and theory to study the energy release mechanisms of decompositions of novel assemblies of gas generators containing nanoscale Al (conventional Al nanoparticles and Al nanoclusters) to overcome the sintering and/or oxide-formation issues. Experimentally, a previously published hypothesis for the mechanism leading to enhanced energy release from Al nanoparticles in the presence of a gas generator was disproven, and a new hypothesis was developed. Computer simulations demonstrated that an unexpected intermixing inhibits the effect of small-scale Al clusters passivated with a gas generator, introducing different hindrances to enhanced combustion.

15. SUBJECT TERMS
aluminum, nanoparticles, laser ignition, molecular dynamics, density functional theory, DRI, Director's Research Initiative

16. SECURITY CLASSIFICATION OF:			17. LIMITATION OF ABSTRACT	18. NUMBER OF PAGES	19a. NAME OF RESPONSIBLE PERSON
a. REPORT	b. ABSTRACT	c. THIS PAGE			N Scott Weingarten
Unclassified	Unclassified	Unclassified	UU	46	19b. TELEPHONE NUMBER (Include area code) 410-306-0718

Contents

List of Figures

List of Tables

Acknowledgments

Dr Batyrev wishes to thank Dr Nirupam Trivedi for his suggestion to model high-energy-content ligands in his density functional theory calculations. The authors collectively wish to thank Dr Betsy Rice for her guidance during the course of the project and her careful reading of this manuscript and the corresponding suggestions. All computational modeling was performed on the Department of Defense Supercomputer Resource Centers at the US Army Research Laboratory, the US Army Engineer Research and Development Center, and the Air Force Research Laboratory.

INTENTIONALLY LEFT BLANK.

1. Introduction

There is an extensive history of research showing that the addition of metal particles to explosives and propellants can greatly improve their performance (Gottfried 2012). For example, aluminum (Al) powder, on the order of 10s of microns in diameter, results in an increase in the heat of explosion and higher temperatures (Politzer et al. 2001). Nanoparticle fuels offer the possibility of even faster energy release, more efficient combustion, and controllable explosive performance (Brousseau and Anderson 2002; Dlott 2006). However, formulations containing Al nanoparticles (np) generate significantly less energy than expected because of the formation of oxide layers on the Al and sintering of the np during chemical reactions.

To avoid these issues, the original goal of this project was to investigate mesoparticle assemblies consisting of near-metallic state Al atomic clusters (e.g., Al_{50}) passivated with an energetic gas generator. Attempts to synthesize such clusters using a custom-designed metal halide condensation reactor were unsuccessful. An electrospray method was used to create 2 alternative types of mesoparticles, with the hypothesis that these assemblies would provide a more intimate mixture of the formulation ingredients, resulting in increased energy release following ignition. The experimental focus of this report is on the results of laser ignition of these mesoparticles.

The computational modeling aspect of the project remained focused on testing the initial proposal of increased performance from Al nanoclusters. The results of classical molecular dynamics (MD) simulations of mesoparticle assemblies of Al_{50} nanoclusters in a gas generator composed of 5-aminotetrazole (5-ATZ) are reported, as are density functional theory (DFT) calculations of Al and cyclotrimethylene trinitramine (RDX).

2. Experiment

2.1 Mesoparticle Assembly and Disassembly

Mesoparticles were synthesized by conventional spray pyrolysis (CSP) in which precursor solutions of suspended np and an ionized gas generator were atomized into a carrier gas flowed into a silica gel dryer and tube furnace and sent to an electrostatic nanoaerosol sampler and/or membrane filter for particle collection. Evaporation of the precursor solvent in each droplet nucleated a mesoparticle of agglomerated np and precipitated gas generator.

Various diagnostic techniques were used to investigate the assembled mesoparticles, including transmission electron microscopy (TEM) with energy dispersive spectroscopy (EDS) for elemental analysis and low-rate in situ sample heating and scanning electron microscopy (SEM) with EDS and high-rate in situ sample heating; these techniques enabled the assessment of the mesoparticle morphology, composition, and behavior upon heating. A differential mobility analyzer was also used to measure particle size distributions reliably at particle diameters greater than 10 nm. Thermogravimetric analysis (TGA) and differential scanning calorimetry (DSC) were used to investigate material decomposition with temperature and time-of-flight mass spectroscopy to analyze gaseous species produced upon high-rate heating.

The conventional np chosen for the initial stage of this project were silica (SiO_2) particles with diameters of 10–20 nm, since they are easily sensed by aerosol particle counters. The inert metallic particles used were various polyoxometallates (POMs) of 1–2 nm diameters. These are similar in size and morphology to energetic clusters, which are prohibitively difficult to sense by aerosol particle counters. The POMs are polyatomic ions composed of oxyanions assembled in a framework by shared oxygen (O) atoms. The gas generators employed were tetrazole (TZ) molecules composed of energetic ligands with large heats of formation, which decompose largely into high volumes of innocuous nitrogen gas and require minimal O consumption.

In the first year, 3 TZ molecules were evaluated using TGA/DSC, and mesoparticles of $SiO_2$and TZs were synthesized by CSP. EDS results showed that only 4.7%–8.7% of the TZ added to the precursor was deposited in the particle by this method. Furthermore, TEM with low-rate in situ heating revealed that gas was generated slowly in the mesoparticles, which deformed only slightly to release the internal pressure. It was hypothesized that a high heating rate is necessary to achieve higher internal mesoparticle pressures in a much shorter time scale. SEM with high-rate in situ heating observed minimal to no change in mesoparticle morphology and size before and after heating, suggesting that the resulting internal pressure impulse created upon TZ decomposition was not able to catastrophically eject the nanoparticle primaries.

The substitution of smaller 1- to 2-nm POMs for the SiO_2 nanoparticle primaries produced similar results. EDS results varied with different POMs and TZ molecules but on average showed 5%–10% of the TZ in the precursor was deposited in the mesoparticles. Most compositional variation occurred at the outer edge of the mesoparticles with TZ concentration reaching as high as 112% of the concentration in the precursor solution in the most extreme case (30% on average). This evidence suggested outward diffusion of the TZ during the CSP synthesis process. TEM and

SEM with in situ heating results were largely consistent with the SiO_2results. Low-rate heating showed slow TZ decomposition and particle deformation upon the gas release (Fig. 1). An instance of particle ejection was observed to a small degree upon high-rate heating to approximately 290% of the TZ decomposition temperature, accompanied by sintering of the ejected POMs (Fig. 2).

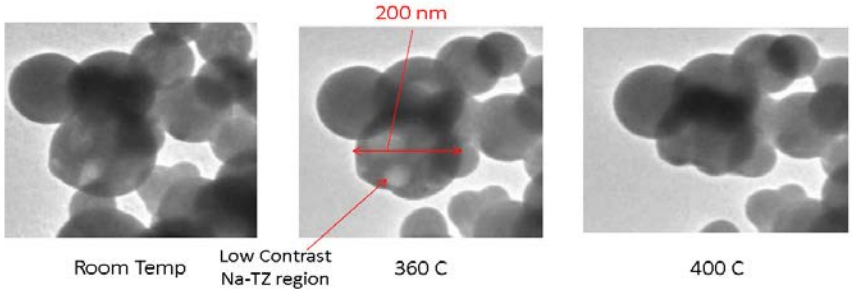

Fig. 1 POMs and TZ TEM with low-rate heating

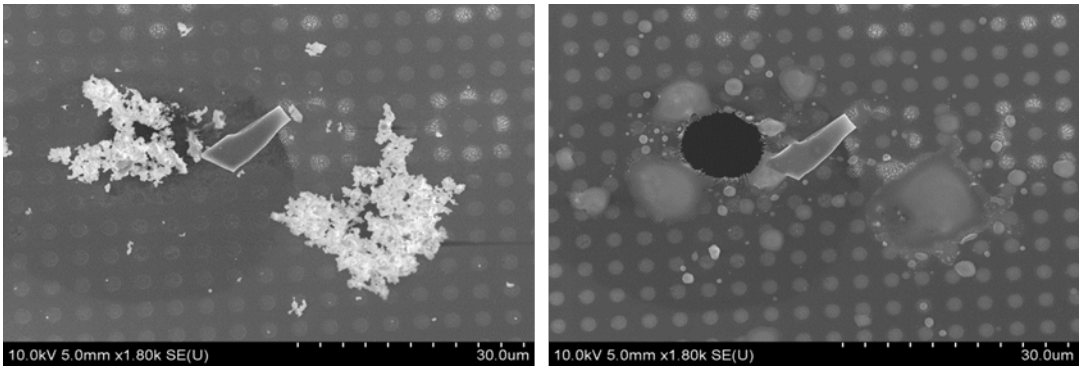

Fig. 2 POMs and TZ SEM with high-rate heating at room temperature (left) and after 20 ms at 700 °C (right)

Some observations using the SiO_2 or POMs also showed separation among the nanoparticle primaries and the gas generator, including contrast and compositional variations within particles in micrographs and micron-sized features of TZ agglomerations among the mesoparticle population (Fig. 3).

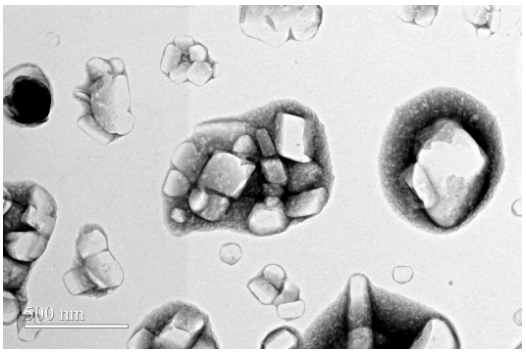

Fig. 3 POMs and TZ with a high TZ loading

2.2 Laser Ignition of Nanoaluminum Formulations

In years 2 and 3, laser ignition was explored as an alternative method for rapid heating of the mesoparticles. Nanosecond-pulsed laser ignition offers the advantages of noncontact ignition with adjustable energy transfer at high heating rates, 10^{12}–10^{13} K/s. Since the laser-induced plasma heats the materials well above their melting or decomposition temperatures, laser ignition is well suited for studying the kinetics of the ensuing vapor phase reactions. For this phase of the project, 2 alternative types of mesoparticles were obtained, one containing conventional 50-nm Al np with 10% nitrocellulose (NC) (Wang et al. 2013) and a second containing Al (50 nm) and copper oxide (CuO) (50 nm) with 5% NC (Wang et al. 2014). Identical precursor suspensions were prepared for each sample, resulting in physical mixtures of the formulations for comparison to the electrosprayed (ES) mesoparticle assemblies. Two batches of the 4 samples were prepared (batch 1 was received in February 2014 and batch 2 was received in August 2014); a description of the samples and the nomenclature used in this report is shown in Table 1.

Table 1 Description of samples tested

Sample	Description
PM Al/NC	Physical mixture of 50-nm Al and 10% NC
ES Al/NC	Electrosprayed mesoparticle of 50-nm Al and 10% NC
PM Al/CuO/NC	Physical mixture of 50 nm Al, 50-nm CuO, and 5% NC
ES Al/CuO/NC	Electrosprayed mesoparticle of 50-nm Al, 50 nm CuO, and 5% NC

PM = physically mixed

The hypothesis was that the mesoparticle assemblies would provide a more intimate mixture of the formulation ingredients, resulting in increased energy release following laser ignition.

The energy release of the samples shown in Table 1 was compared using several different experimental techniques. For one experiment, a pulsed laser (Nd:YAG, 1064 nm, 6 ns, 900 mJ) was focused onto each sample to induce a deflagration reaction involving ejected particles in the air above the sample residue, which was affixed to double-sided tape on a glass slide (Fig. 4). Both the time-resolved emission (via an infrared [IR] photoreceiver from 900 to 1,700 nm and a visible photoreceiver filtered at 480 ± 5 nm to observe AlO) and the wavelength-resolved emission (gated at 100 ms) were recorded, and 2-color optical pyrometry with high-speed cameras filtered at 700 and 900 nm was used to measure the temporally and spatially resolved temperatures of the particle reaction following ignition.

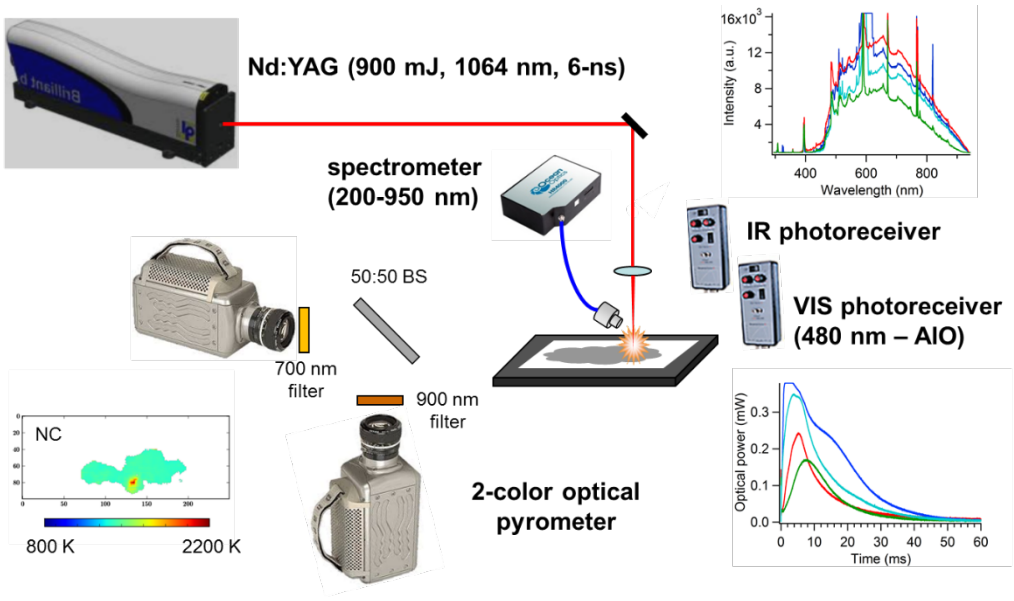

Fig. 4 Laser-induced deflagration setup with emission spectroscopy, time-resolved emission detection, and 2-color optical pyrometery using high-speed cameras

The wavelength-resolved spectra from samples in both batches showed broad emission from the burning of condensed particles in the deflagration region in addition to the discrete emission features due to Al, AlO, Cu, hydrogen (H), nitrogen (N), oxygen (O), and various contaminants (Fig. 5); the presence of metal contaminants (e.g., iron and magnesium) in the physical mixtures (but not in the mesoparticles) was noted—this contamination was likely incurred during sample handling (e.g., from a metal spatula). The time-resolved emission traces from samples in batch 2 (Fig. 6) suggest higher (and faster) peak energy release for ES Al/NC compared to the PM Al/NC, indicating that the mesoparticle Al/NC sample combusted much more efficiently than the physical mixture. The initial sharp increase in emission (<100 μs) is due to the laser-induced plasma. The secondary emission peaks (>500 μs) result from the subsequent chemical reactions after the plasma has cooled, leaving the ejected particles to react in the heated air. As expected, the Al/CuO/NC samples produced more significant energy release than the Al/NC samples; however, the ES Al/CuO/NC peak intensity was lower than that of the PM Al/CuO/NC and slightly delayed in time (by several milliseconds). This delay could be caused by a confinement effect in the mesoparticle samples, where the heat of reaction builds up in the mesoparticle before it falls apart. Interpreting these results was difficult since the set of samples prepared in batch 1 had a different source of Al np and resulted in much more rapid reaction of the Al/CuO/NC samples (<6 ms), with comparable total energy release between the PM and ES Al/CuO/NC particles; the ES Al/NC from the batch 1 samples had a

peak energy release 3.5 times that of the PM Al/NC from batch 1, a slight increase in the enhancement shown in batch 2 (Fig. 6).

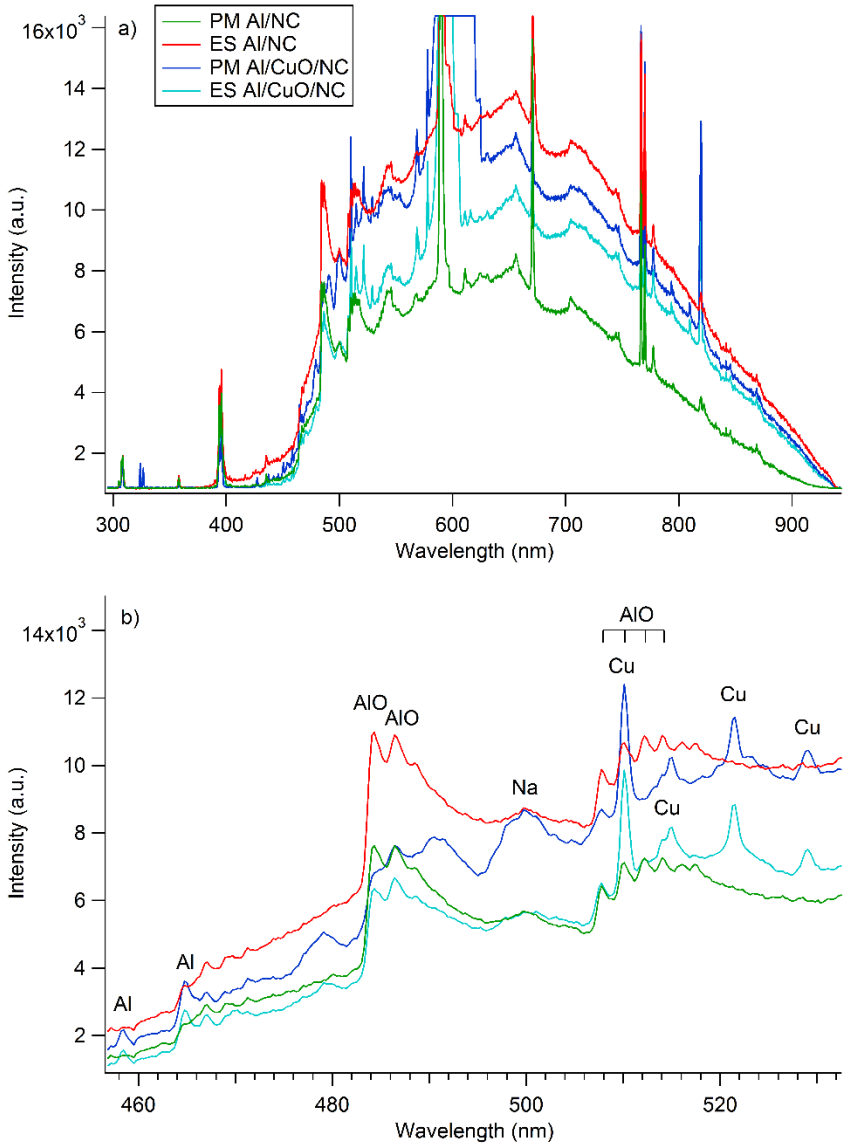

Fig. 5 Emission spectra from the PM and ES Al/NC and Al/CuO/NC samples from batch 2, including a) the broadband spectra showing the broad emission from burning condensed phase particles and b) a zoomed in region showing discrete emission features from Al, Cu, and the sodium contaminant

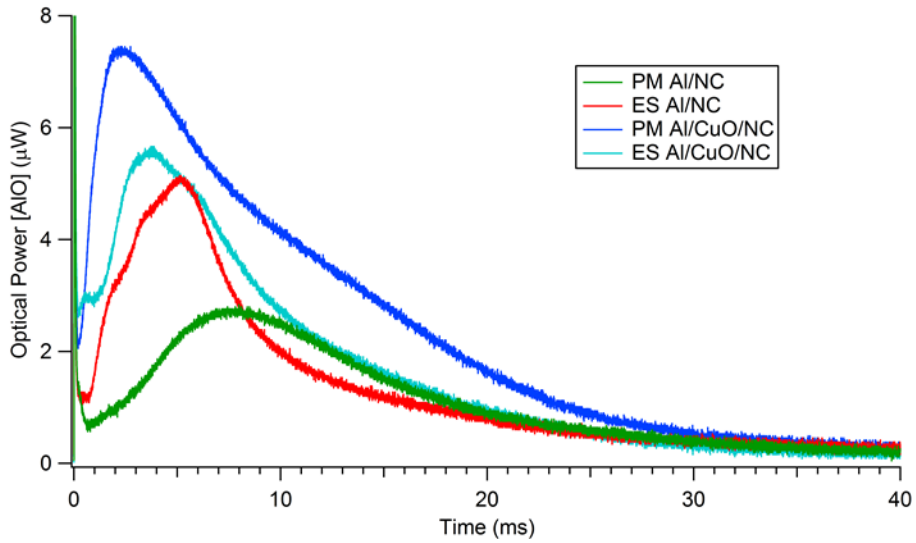

Fig. 6 Time-resolved AlO emission from the laser-induced deflagration of nano-Al formulations in batch 2 (similar trends were observed with the IR photoreceiver)

Optical pyrometry with 2 high-speed cameras was used to produce spatially and temporally resolved temperature maps of the laser-induced deflagrations. Fig. 7 shows snapshots from the high-speed imaging of the Al/CuO/NC samples from batch 2, along with the corresponding temperature maps. The high-speed video images and temperature maps show distinct differences between the physical mixtures and mesoparticles. The physical mixtures have higher temperatures on the outside surfaces of the deflagration cloud and have significantly more scattered individual particles burning, while the mesoparticles show larger regions of higher temperature inside the deflagration cloud. This suggests that the Al np are significantly oxidized by the surrounding air in the physical mixtures, but for the electrosprayed samples, the Al nanoparticle oxidation occurs primarily within the mesoparticle assemblies at earlier times (i.e., the reaction chemistry is more confined). The NC coating holds the np together longer and delays their reaction with atmospheric O_2. This is in direct contrast to the hypothesis put forward by (Wang et al. 2013) that the O_2 is able to diffuse through the NC coating and react with the Al nanoparticle. Instead, the Al np appear to be initially reacting with either the NC and/or the CuO in the mesoparticle assemblies, until the NC eventually decomposes. Reaction of the atmospheric O_2 with the remaining unoxidized Al np occurs at much later times (>10 ms), resulting in a significant temperature increase and extended combustion times (especially for the ES Al/NC).

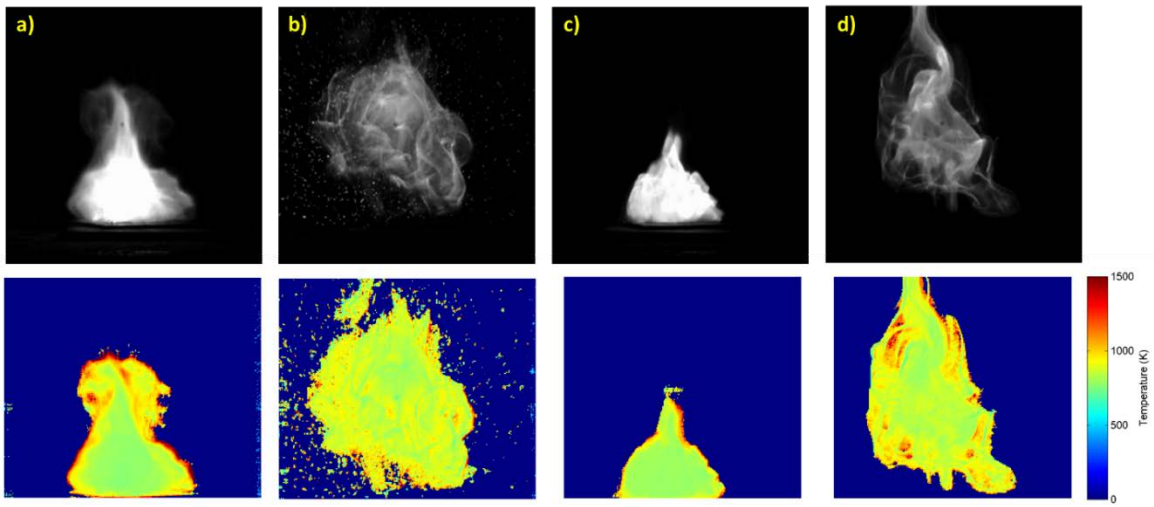

Fig. 7 Snapshots from the high-speed video of the laser-induced deflagration of PM Al/CuO/NC at a) 1.6 ms and b) 10 ms and ES Al/CuO/NC at c) 1.6 ms and d) 10 ms

The spatially averaged temperature from each video frame was calculated, and the results are shown in Fig. 8. The initial temperature for the PM Al/CuO/NC sample is higher than the corresponding ES sample, but the confinement effect of the mesoparticles results in the temperature continually increasing in time for the ES sample while the PM sample cools. Similarly with the Al/NC samples, the initial temperature is lower with the ES sample than the PM sample, but the reaction lasts significantly longer.

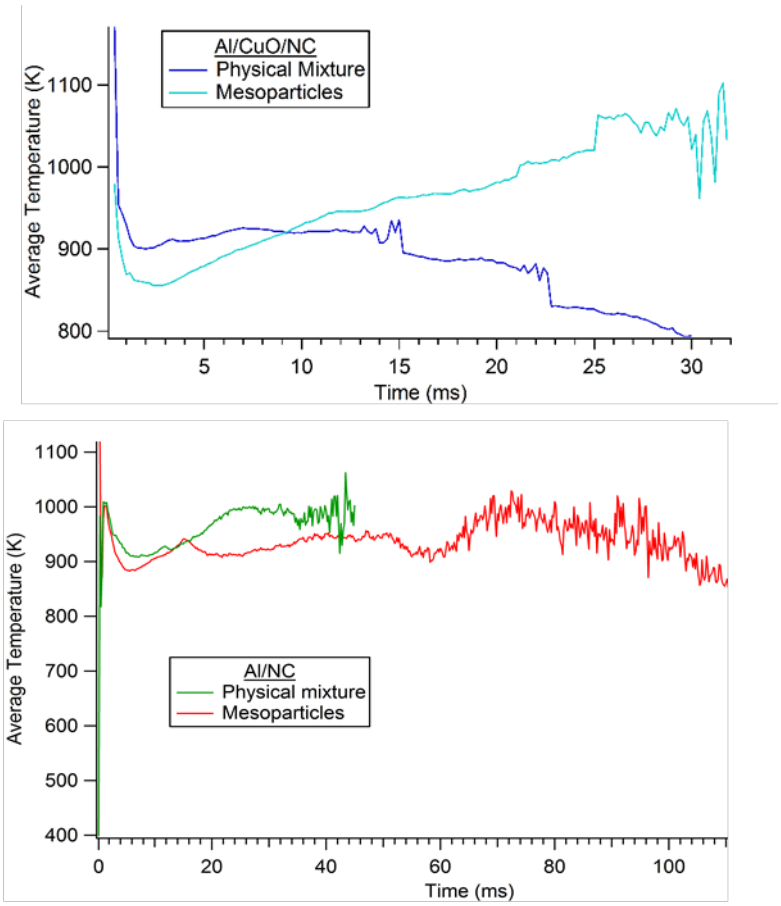

Fig. 8 Spatially averaged temperatures for the laser-induced deflagration of Al/CuO/NC (top) and Al/NC (bottom) samples

Confined nanosecond-pulsed laser ignition experiments were performed on batch 1 of the Al/CuO/NC (a more reactive set of samples than batch 2) in a 500-mm chamber with a pressure transducer port (Gottfried et al. 2014). While the mylar burst disk (designed to break at around 700 psi) did not break following ignition of the PM Al/CuO/NC, it burst 50 μs after ignition of the ES Al/CuO/NC sample (Fig. 9). In comparison, the deflagration of pure NC is extremely weak; its pressure generation is also shown in Fig. 9. A year later, additional confined ignition tests were performed with a variable pulse width laser (Nd:YAG, 1064 nm, 10 ms, 5 J) on both sets of samples (batch 1 and batch 2). This time, the mylar disk did not burst for any of the samples; however, the Al/CuO/NC samples reacted faster (and stronger) than the Al/NC samples (Fig. 10). The peak pressure for the ES Al/NC sample was higher than that of the PM Al/NC (consistent with the laser-induced deflagration results). The Al/CuO/NC samples from batch 2 (PM and ES) reached their peak pressures around 2.7 ms (not shown, compared to 35 μs for the samples in batch 1).

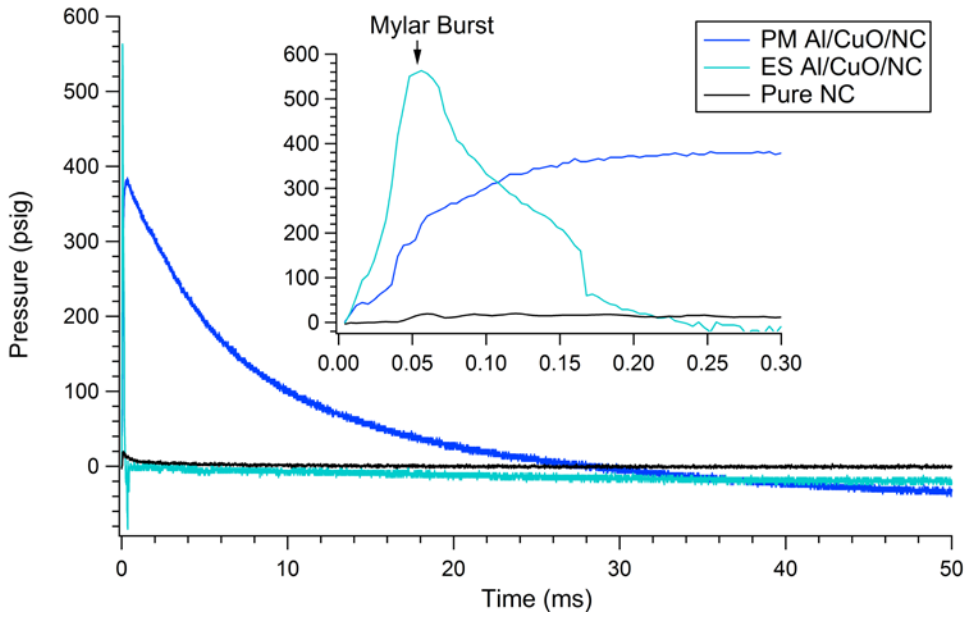

Fig. 9 Peak pressures achieved through confined nanosecond-pulsed laser ignition of the Al/CuO/NC samples from batch 1

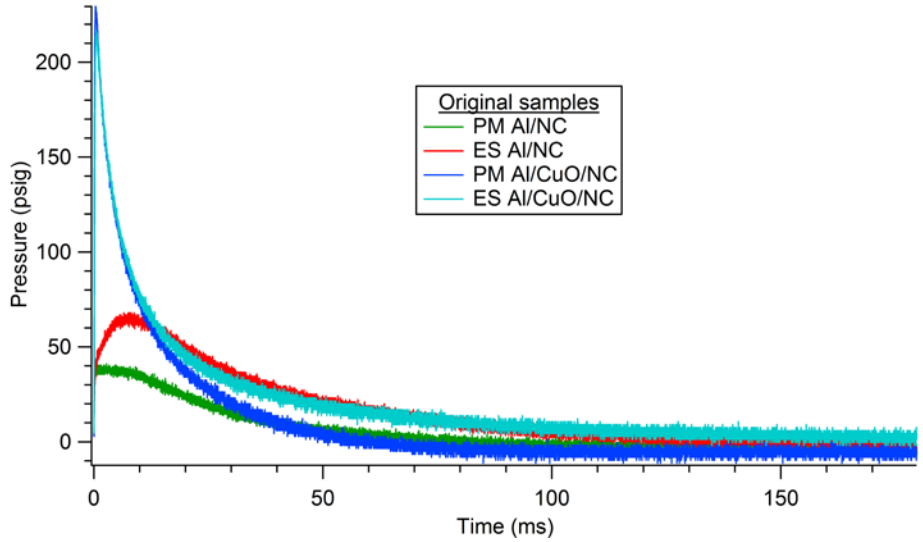

Fig. 10 Peak pressures achieved through confined millisecond-pulsed laser ignition for samples from batch 1

Finally, schlieren imaging was used to measure the shock wave resulting from the laser-induced plasma generated during pulsed laser ignition. When exothermic reactions occur in the laser-induced plasma, the increased plasma temperature results in faster shock wave propagation. Thus, the extent of the energy release in the laser-excited material can be correlated to the shock wave velocity (Gottfried 2014). The shock velocities for the original samples (batch 1) showed an increase

in fast energy release (during the first several microseconds of the laser-induced plasma) for the mesoparticle samples, especially the ES Al/CuO/NC (Fig. 11). In contrast, experiments on samples from batch 2 demonstrated that the fast energy release was comparable between the PM and EM samples for both Al/NC and Al/CuO/NC (Fig. 12). The reacted residues were excited with the laser following laser ignition of the samples and produced significantly lower shock velocities, indicating most of the chemical energy had already been expended, as expected. The emission spectra of the reacted residue did not show the broad emission from the condensed phase particles reacting, instead, strong atomic emission from Al and Cu was observed (Fig. 13).

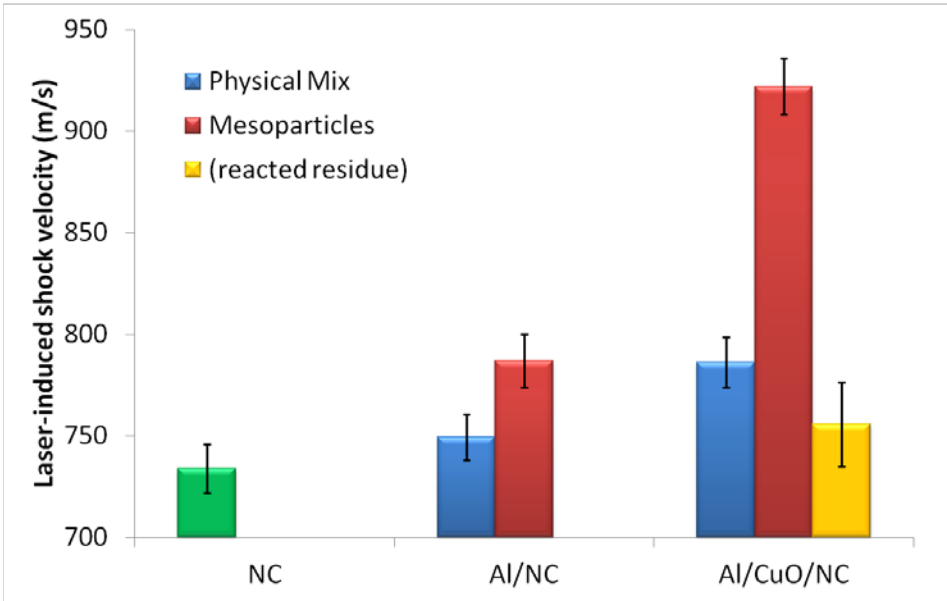

Fig. 11 Laser-induced shock velocities for the pure NC and batch 1 samples (PM and ES Al/NC, PM and ES Al/CuO/NC); the ES Al/CuO/NC had significantly more energy content than the PM Al/CuO/NC

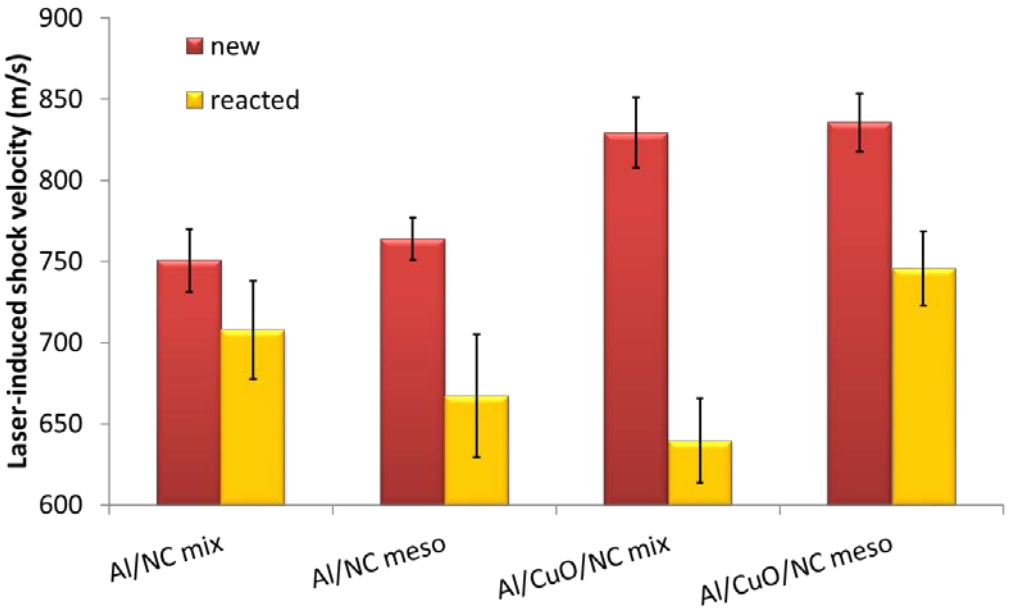

Fig. 12 Laser-induced shock velocities for the 4 samples investigated (batch 2) and the residue remaining after the laser-induced reaction

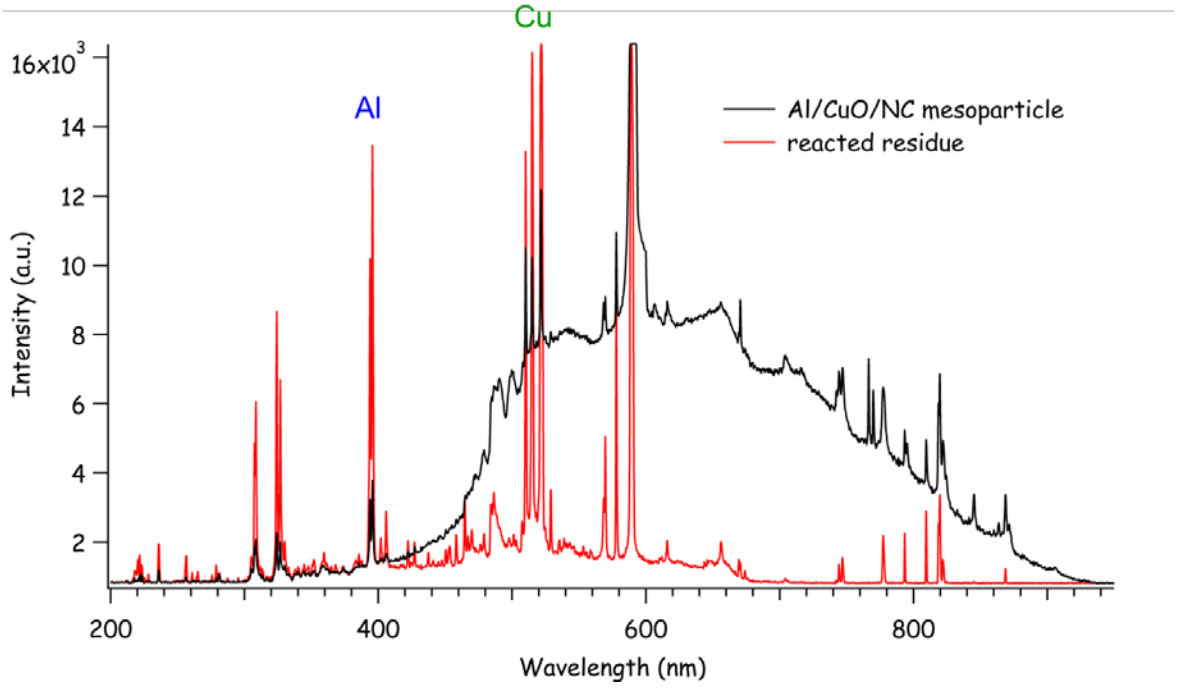

Fig. 13 Emission spectra of unreacted (black) and reacted (red) ES Al/CuO/NC

3. Quantum Mechanical Simulations

3.1 Al Nanoclusters Passivated with High-Energy-Content Ligands

This section presents the results of high-fidelity quantum mechanical methods to determine whether Al nanoclusters could be suitably passivated with high-energy-content ligands and to determine the fate of fragments emanating from a decomposing Al nanocluster.

To elucidate the key mechanisms governing passivation of the Al clusters, we performed DFT calculations on several relaxed structures of Al clusters. From these simulations, we tried to determine the most energetically favorable mechanism of passivation. We passivated Al_{77} by the high energy, high-nitrogen content ligand $C_2H_2N_9$, which is similar to $C_2H_4N_{10}$ (Klapotke et al. 2012) but requires less computational resources due to having fewer atoms. The Al_{77} cluster has 4 surface atoms at both the top and bottom and 3 surface atoms at each of the 4 central sides. We attempted to passivate the top and bottom 8 atoms by 4 ligands and the central surface atoms by 12 ligands. The passivated Al_{77} cluster was relaxed by the density functional theory plane wave method (Segall et al. 2002) with ultrasoft pseudopotentials. The relaxation of the 281-atom model within a 30- × 30- × 30-Å cubic cell with periodic boundary conditions was performed using the generalized gradient approximation (GGA) functional (Perdew et al. 1996) within the PW91 approximation (Perdew et al. 1992). The resulting Al_{77} structure passivated by 16 high-energy-content ligands and charge distribution is shown in Fig. 14.

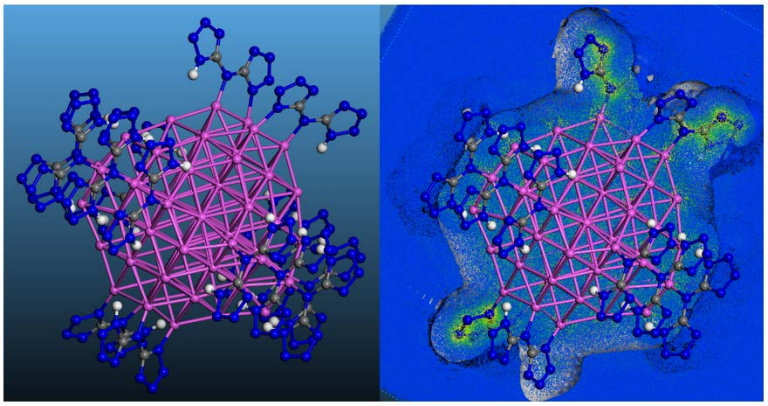

Fig. 14 Al_{77} passivated by high-nitrogen-content ligands. Blue = nitrogen, white = hydrogen, grey = carbon, and pink = aluminum atoms: a) optimized structure and b) charge distribution cross section through the center of the cluster at iso value 0.075.

The calculations indicate that H atoms come closer to the surface of the Al cluster and provide a partial passivation of Al atoms (Fig. 14b). On the other hand, there are subsurface Al atoms whose charge and potential distributions fall outside of the Al cluster, indicating that the cluster is not completely passivated with these ligands. The results indicate the need of Al nanoclusters passivation by smaller molecules like H_2 or cyclopentadienyl Cp* ($C_5[CH_3]_5$) during synthesis. The Cp* ligands were successfully used by Schnoeckel and co-workers (Vollet et al. 2004) for synthesis of 50-atom Al clusters. The bond lengths (BLs) of the cluster depends on the ligands (e.g., Al cluster having 50 atoms with Cp* ligands has the shortest BLs of approximately 3.87 Å [Williams and Hooper 2011]). After removal of the ligands, according to our calculations the Al_{50} cluster shrinks and the BLs in a kernel are approximately 3.4 Å. Local potential and charge distributions of the relaxed Al_{50} cluster are depicted in Fig. 15. Significant potential and charge contribution comes from subsurface atoms (the 5 atoms surrounding a surface central atom).

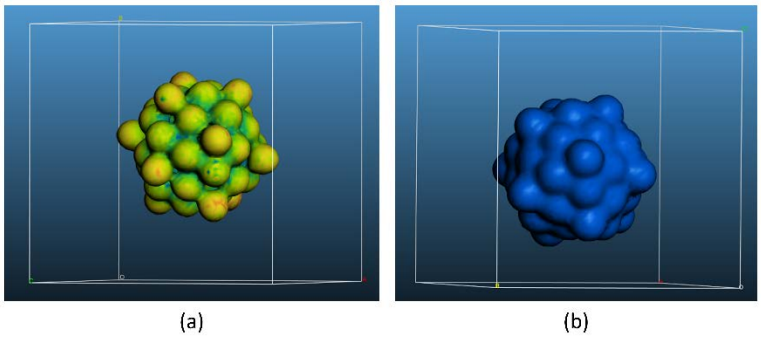

Fig. 15 Local potential a) around an Al50 cluster (iso value 0.04) and b) charge density (iso value 0.01)

4. Molecular Dynamics

4.1 Background

Various classical MD simulations were performed to test the hypothesis presented in the Introduction section, focusing on the disassembly of Al_{50} nanoclusters passivated with 5-ATZ. There have been numerous MD studies of metallic np looking at structure and growth properties (Zeng et al. 2007; Kaur et al. 2011), melting (Sang et al. 2013), sintering (Ding et al. 2009), oxidation (Hong and van Duin 2015), and energetic reactions (Evteev et al. 2009; Henz et al. 2009). More recently molecular np have been considered using MD techniques, looking at self-assembly (Bodnarchuk et al. 2015), deliquescence (Akbarzadeh et al. 2015), and energetics (Alavi et al. 2003). There have also been a number of studies that use

MD techniques to study interactions between solvents and np where the nanoparticle is modeled as a large single particle (or mesoparticle) on the order of nanometers in diameter (i.e., Hattemer and Arya 2015). While these types of simulations allow for larger scale models, they are not fully atomistic which precludes the study of reaction and disassembly, hence we did not pursue such methods.

The ReaxFF-*lg* force field used in this study will be described in Section 4.2. All simulations were performed using the Large-scale Atomic/Molecular Massively Parallel Simulator (LAMMPS) computer code (Plimpton 1995). Unless otherwise noted, the timestep in our simulations is 0.1 fs, and periodic boundaries are employed in all directions.

The Al_{50}/5-ATZ mesoparticles used in this study consist of Al_{50} nanoclusters embedded in a spherical 5-ATZ particle. The means of generating initial configurations of these np for MD simulations will be presented in Section 4.3. The Al_{50} nanocluster has been experimentally synthesized, passivated by cyclopentadienyl ligands (Vollet et al. 2004), and subsequently studied via DFT (Williams and Hooper 2011). The development of these systems stems from similar reasons as ours, namely to pursue surface passivation with organic functional groups that prevent the formation of an oxide layer. The Cp* ($C_5[CH_3]_5$) molecule used in our simulations is shown in Fig. 16a.

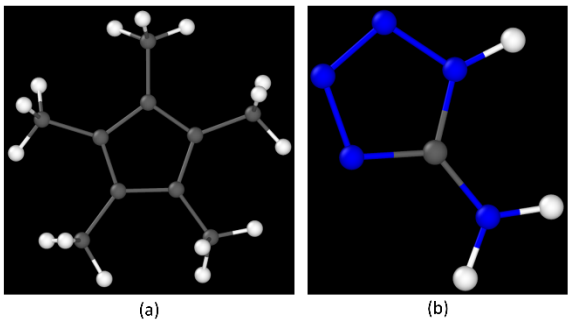

Fig. 16 Structures of the a) Cp* molecule ($C_5[CH_3]_5$), and b) 1H-5-aminotetrazole (ATZ) molecule, (CN_5H_3). All atomistic images in this section were created with OVITO visualization software (Stukowski 2010).

Figure 16b shows the 5-ATZ molecule employed as a gas generator. Considering the high nitrogen content (the chemical formula is CN_5H_3), aminotetrazoles are an important ingredient in gas generating compositions and solid rocket propellents (Williams et al. 1994). The thermal decomposition of 5-ATZ has been extensively studied experimentally (i.e., Lesnikovich et al. 2002) and computationally (Paul et al. 2009). In addition, the crystal structure of 5-ATZ has been investigated, with the 4 molecule unit cell determined as orthorhombic with a space group $P2_12_12_1$ (Fujihisa et al. 2011).

Our MD simulations subject the Al_{50}/5-ATZ mesoparticle to rapid heating to study disassembly. A fairly unique aspect of these nanoparticle simulations is the amount of free space present in the simulation cell. LAMMPS typically partitions space uniformly for simulations run on multiple processors, as depicted in Fig. 17a, where the yellow grid lines represent 16 processors and the atoms belonging to those processors are variously colored. This results in a number of processors having zero atoms (there are 6 such domains in Fig. 17a) leading to highly inefficient use of parallel processing. However, there is a means of balancing the load on multiple processors by adjusting the size and shape of sub-domains in LAMMPS, as shown in Fig. 17b. Now there are only 2 domains with zero atoms and a smaller number of atoms on the other processors. We have employed this capability in our simulations, greatly reducing the necessary computer time to run them.

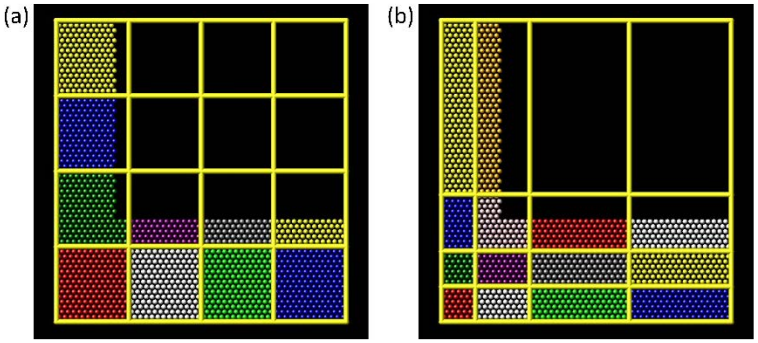

Fig. 17 a) A uniform grid partitioning 2-dimensional space and b) an alternate partitioning that decreases the area where the density of atoms is higher (image from the LAMMPS User Manual, lammps.sandia.gov, used with permission)

In this section, we will describe the reactive interatomic potential that was developed for these simulations and discuss its ability to model the Al_{50} nanocluster and the 5-ATZ crystal structure. A number of methods were devised and tested to generate or assemble the mesoparticles, and the 2 most successful will be described and compared in detail. And finally, the disassembly process is analyzed including a discussion of the implications on the original hypothesis of having access to nano-Al for use is energetic formulations.

4.2 ReaxFF-*lg*

All simulations in this section were performed using ReaxFF-*lg*, which is a widely used reactive force field that was developed to model hydrocarbons (van Duin et al. 2001) and has subsequently been fitted to model a variety of systems (i.e., Liu et al. 2011). The force field is based on a bond order/bond distance relationship, which is subsequently used to determine the overall system energy from numerous partial energy contributions:

$$E_{\text{ReaxFF}} = E_{bond} + E_{lp} + E_{over} + E_{under} + E_{val} + E_{pen} + E_{coa} + E_{tors} + E_{conj} + E_{H-bond} + E_{vdW} + E_{Coulomb} + E_{\text{lg}}, \quad (1)$$

where the terms represent bond energy (*bond*), lone pair energy (*lp*), corrections for atom overcoordination (*over*) and undercoordination (*under*), valence angle energy (*val*) including a penalty function (*pen*), angle conjugation energy (*coa*), torsion angle energy (*tors*), torsion conjugation energy (*conj*), hydrogen bond energy (*H-bond*), van der Waals energy (*vdW*), Coulomp energy (*Coulomb*), and long range dispersion correction (*lg*). One significant hindrance in using ReaxFF-*lg* is the large number of parameters that need to be fit and the challenges associated with obtaining adequate parameter sets (Larentzos et al. 2015; Rice et al. 2015).

The ReaxFF-*lg* force field used in our simulations is a combination of a parameter set for C-H-N-O energetic systems (Liu et al. 2011) and a recently developed set for modeling aluminum and aluminum oxide (Sen et al. 2013). To test this force field for use in Al_{50}/5-ATZ systems, we simulated the $Al_{50}Cp^*_{12}$ nanocluster in the microcanonical (NVE) ensemble with initial velocities assigned to correspond to a temperature of 300 K. The cluster, with initial atomic positions obtained from DFT (Williams and Hooper 2011), is at the center of a large simulation cell with periodic boundaries. Figure 18a shows this initial configuration. The outer layer of Al atoms is arranged such that peaks appear in the Al_{50} nanocluster. There are 12 of these peaks and a Cp* molecule is centered at each of them. The equilibrated structure from MD is shown in Fig. 18b. Clearly, the Cp* molecules have moved away from the Al_{50}, resulting in a more spherical nanocluster, although the shape remains largely the same. This is verified in Fig. 18c, which is an expanded view of the nanocluster that includes yellow arrows that indicate the displacement of the atoms from the initial configuration. The largest displacement of Al atom is a mere 1.18 Å. We are interested in embedding the Al_{50} nanocluster in 5-ATZ, not Cp*, so the differences between Figs. 18a and 18b are not important. The ReaxFF-lg potential does an excellent job of modeling the Al_{50} nanocluster.

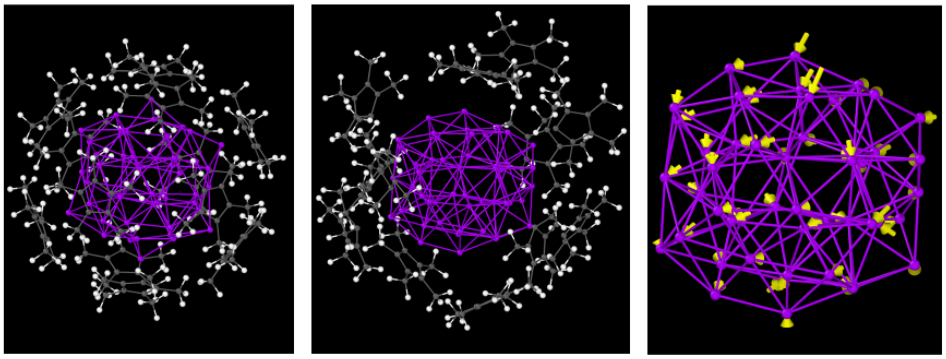

Fig. 18 a) Structure of $Al_{50}Cp_{12}$* obtained from DFT, b) final configuration from MD, and c) the positions of the Al atoms from MD with overall displacements relative to DFT indicated by yellow arrows

As for the potentials ability to model 5-ATZ, we performed an MD simulation on a system containing 9 × 13 × 3 unit cells, resulting in 1,404 molecules (12,636 atoms). The initial configuration, with experimental atomic positions, is shown in Figs. 19a and 19b projected onto the xy- and yz-plane, respectively. The system is equilibrated according to an algorithm developed specifically for ReaxFF-*lg* force fields (Larentzos et al. 2015): NVE for 2.5 ps with velocity scaling every time step; canonical (NVT) at a temperature of 300 K for 2.5 ps; isothermal-isobaric (NPT) at zero pressure and 300 K for 2.5 ps, wherein the lattice constants are unconstrained but the angles are held fixed; and full isothermal-isostress (NsT) at zero pressure and 300 K for 20 ps, during which both the lattice constants and angles are free to change. Configuration data are output every 0.05 ps and averaged over the last 100 configurations (5 ps). The averaging is done in both space and time, such that an average of the 351 unit cells in the configuration are obtained and then averaged over the final 5 ps time interval. This provides us with an overall average unit cell and averaged positions of the 36 atoms in the unit cell, as pictured in Figs. 19c and 19d. The darker atoms represent the experimental atomic positions and the lighter atoms are the average from MD. In Fig. 19c we see that the 2 molecules near the bottom of the unit cell (Molecules 1 and 3) align rather well, but the locations of the molecules near the top differ. It appears that the rings in the 4 molecules want to align vertically from the ReaxFF-*lg* potential. However, Fig. 19d shows the tilt of the molecules is maintained correctly, although once again the molecules tend to align vertically. Table 2 quantifies this discussion, comparing the lattice vectors, density, and positions of the molecular centers of mass. The lattice constants and angles from MD are in excellent agreement with experimental values, as is the density. The average positions of the molecules are correct in the

z-direction in the MD simulations but as mentioned they tend toward the center of the simulation cell in the x- and y-directions, differing considerably from the experimental result. Finally, as seen in Fig. 19, the shape of the molecule is perfect, reflecting the planar nature of the experimental shape and capturing the correct BLs and angles.

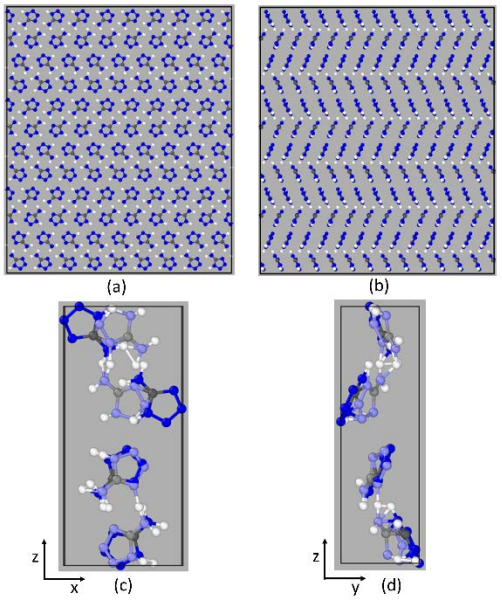

Fig. 19 Experimental crystal structure, with atoms projected onto the a) xz- and b) yz-plane. An overlay of the atomic positions in the average unit cell from MD (light atoms) and the experimental unit cell (dark atoms) projected onto the c) xz-plane and d) yz-plane.

Table 2 Comparison of averaged unit cell and molecular centers of mass positions for 5-ATZ from experiment and MD simulations

Property	**Experiment (Å)**			**MD (Å)**		
a	5.088			4.753		
b	3.664			3.867		
c	18.04			17.982		
α	90.0			89.91		
β	90.0			90.35		
γ	90.0			89.45		
Density	1.68 g/cm^3			1.71 g/cm^3		
Position	***x***	***y***	***z***	***x***	***y***	***z***
Molecule 1	2.77	1.79	6.81	2.39	2.16	6.67
Molecule 2	0.23	3.70	11.23	2.30	2.56	11.34
Molecule 3	2.32	–0.04	2.23	2.43	1.29	2.32
Molecule 4	4.86	1.87	15.84	2.49	1.68	15.67

A better potential for our system of interest could certainly be obtained via fitting, but this is not a trivial procedure. Since we are interested in testing the hypothesis that nanoscale Al would be available upon disassembly of a mesoparticle

containing a gas generator, our initial requirements were that the potential 1) be reactive to model at least rudimentary chemical processes, 2) accurately model the structure of Al nanoclusters, and 3) accurately model the molecular and crystal structure of the gas generator. Of these requirements, only the 5-ATZ crystal structure of the ReaxFF-*lg* model is deficient, although it does accurately predict the unit cell and density.

4.3 Creating Mesoparticles

Many attempts at creating an initial configuration of an Al_{50}/5-ATZ mesoparticle were endeavored; however, the discussion here is limited to the 2 most promising. They can essentially be described as cutting out a particle from bulk crystal and an alternate method employing self-assembly. The former is typically used in generating metal np (Shen et al. 2013), while molecular self-assembly has become a burgeoning field with research encompassing multiple disciplines on materials science. MD techniques have been used to study self-assembly but typically using mesoparticles (as discussed in the previous section) instead of fully atomistic systems (Knorowski et al. 2011).

The self-assembly process used in this study involves a 2-step procedure. First, a single Al_{50} nanocluster is passivated with 5-ATZ molecules initially in a gaseous state. The simulation progresses in the NVE ensemble with each 5-ATZ molecules held rigid. This is shown in Fig. 20a, with the resultant single nanoparticle shown in Fig. 20b. At this stage the simulation is continued with full flexibility of the molecules to equilibrate the nanoparticle. Finally, all molecules with center of mass outside a 15-Å radius are removed leaving the final nanoparticle seen in Fig. 20c.

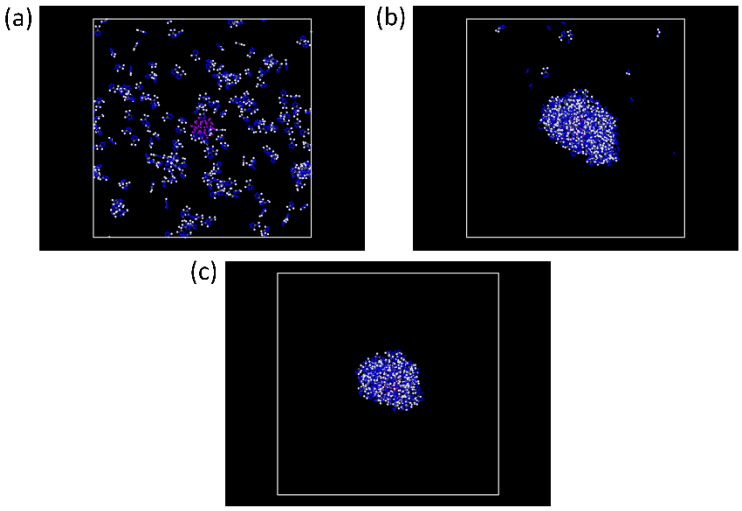

Fig. 20 a) Al_{50} nanocluster (purple atoms) at the center of a simulation cell in a gas of 5-ATZ molecules, b) subsequent growth of the nanoparticle, and c) removal of molecules outside a radius of 35 Å.

The second step in the process is to replicate the nanoparticle seen in Fig. 20c to generate a "gas" of 18 np, which is subject to accumulation to form a mesoparticle. This process is captured in Fig. 21. The initial configuration is shown in Fig. 21a, wherein all the atoms in each individual nanoparticle are given the same random initial velocity and the molecules are once again held rigid. A subsequent image of the nanoparticle "gas" is seen in Fig. 21b. Unfortunately, while promising, we had insufficient time to complete the process, although this is an excellent jumping off point for future endeavors.

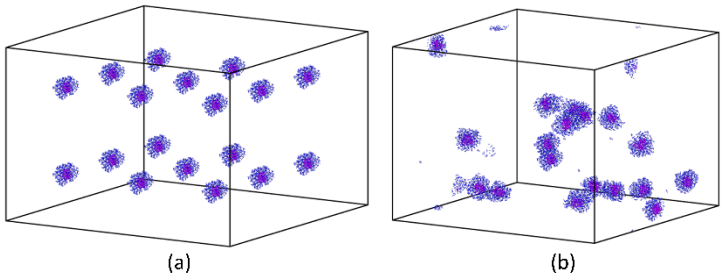

Fig. 21 a) The nanoparticle in Fig. 19 is replicated 18 times. Each nanoparticle is assigned a random velocity resulting in b) a "gas" of nanoparticles.

The second method of generating a mesoparticle starts with crystalline 5-ATZ, from which a sphere with a radius of 35 Å is cutout. Within this crystalline sphere, 15 spherical voids are created with a radius of 7 Å, and the Al_{50} nanocluster is positioned at the center of the voids. The voids are distributed randomly or in a uniform pattern as shown in Fig. 22.

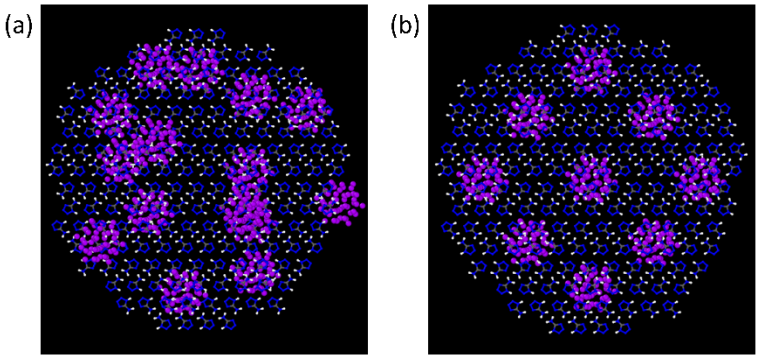

Fig. 22 Initial configurations of the cutout mesoparticles with Al_{50} nanoclusters in a) random and b) uniform distributions. Radius of the spheres is 35 Å.

In both cases, the total number of atoms in the system is approximately 20,000. The equilibration process for the 2 types of mesoparticles differs only because the self-assembly process uses equilibrated np in the formation of the mesoparticle. Once assembled, this system is immediately subjected to the temperature increase described in Section 4.4. As for the cutout mesoparticle, the system is equilibrated as follows: NVE with velocity scaling every time step for 10 ps, NVT at 300 K for 20 ps, and NVE with no velocity scaling for 20 ps. For both cases, the simulation cell is periodic in all 3 dimensions, hence a large vacuum region is introduced around the particle. This also precludes the use of the NPT ensemble.

4.4 Mesoparticle Disassembly

The self-assembled and cutout mesoparticles, having been equilibrated at 300 K, are subsequently subjected to a constant linear temperature increase via NVT-MD to a final temperature of 1500 K over 100 ps. This serves to break apart the mesoparticle, after which the simulation is run in the NVE ensemble until the largest fragments reach the periodic boundaries.

Figure 23 shows the initial and final configurations of the uniform cutout mesoparticle, and Fig. 24 shows the same for the random cutout. In both figures, Al atoms are slightly larger to see the nanoclusters. The images shown in Figs. 23b and 24b are very similar indicating that the initial configuration appears to not be important, although larger simulations would be needed to verify this. In both cases the dispersal of the Al atoms is not uniform for 2 reasons. First, the 5-ATZ mesoparticle is not isotropic since it was formed from the crystalline state which is not symmetric in all directions. Also, the Al_{50} nanoclusters do not remain separated, as seen in Figs. 23c and 24c, which both show a cluster containing more than 50 Al atoms.

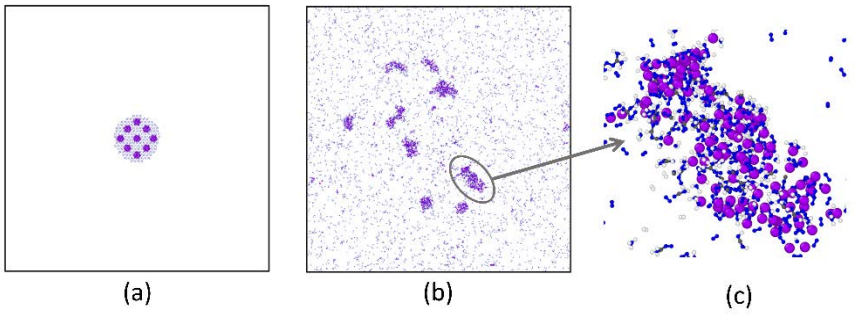

Fig. 23 a) Initial configuration of uniform cutout mesoparticle, b) after subsequent heating, and c) enlarged view of the indicated nanocluster after disassembly

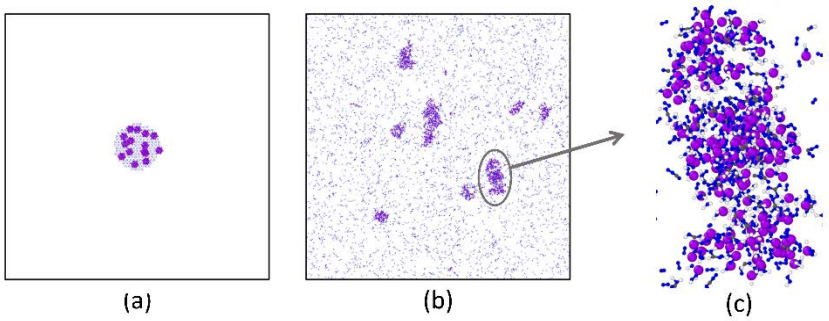

Fig. 24 Same as Fig. 23 for the random cutout mesoparticle

The most important result from Figs. 23c and 24c is that the Al is observed to intermix with the gas generator making it unavailable for further reaction. Recall that the original hypothesis was that Al nanoclusters (such as the Al_{50} used in our simulations) embedded within a gas generator mesoparticle would preclude sintering. Hence, the presence of nanoscale Al would allow for improved performance when incorporated into an energetic formulation. Our simulations indicate that this may not occur due to reaction with Al and the gas generator used to passivate the Al nanoclusters.

The random mesoparticle was also heated in an O environment, the results of which are seen in Fig. 25 (from a different viewing perspective than Fig. 24). The vacuum around the particle is filled with O_2 molecules at a density equivalent to the density of air. The disassembly of the mesoparticle is similar, although fewer clusters are observed in Fig. 25b. Fig. 25c shows that an O_2 molecule was able to penetrate the largest of these nanoclusters.

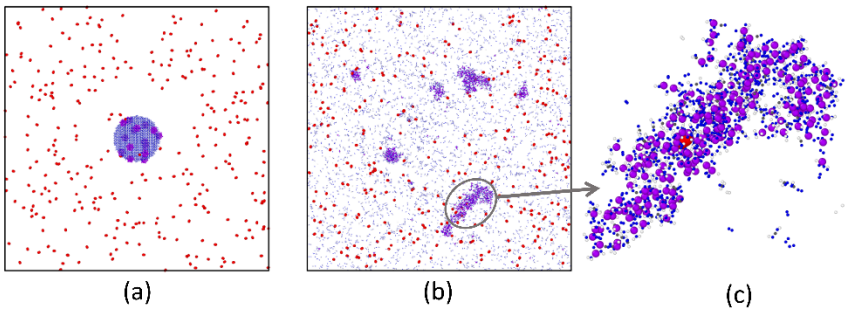

Fig. 25 Same as Fig. 24 with random cutout mesoparticle initially in O

5. First Principles Molecular Dynamics

5.1 Computational Methodology

Consistent with the goals of the MD simulations of the previous section, it is of interest to know the fate of hot reactive small Al clusters ejected from a gas generator mesoparticle. In this section we present results of QM modeling of the interaction of Al atoms, dimers, and trimers with a conventional CHNO energetic material: RDX, which is commonly used in explosive formulations.

Quantum mechanical MD simulations were performed using Gaussian and plane waves as implemented using the cp2k software suite (version 2.6.2) (Hutter et al. 2014) using DFT with orbital transformations (OTs) and the conjugate gradient (2-point line search) method of orbitals optimization. For carbon, O, N, H, and Al atoms we used the double-zeta valence polarized (DZVP-GTH) basis set and Goedesker-Teter-Hutter (GTH) pseudopotentials (Goedecker et al. 1996). The surface [210] of RDX was chosen for simulations since this is one of the most stable experimentally established surfaces of crystalline RDX (ter Horst et al. 1999). Atoms at the back surface of the RDX unit cell containing 168 atoms were held fixed, and 14 Å of vacuum was introduced above the top surface of the RDX crystal. The space was sufficient to accommodate Al atoms at various areas of the "rough" RDX surfaces (Figs. 26a, 27a, and 28a). NVT DFT MD simulations were performed at 100 °C for up to 2 ps using a step size of 1 fs and using the Nose Hoover thermostat with time constant of the thermostat chain of 1,000 fs. We also performed test calculations with step size of 0.5 fs since the system contains hydrogen atoms, and usually MD simulations require smaller steps sizes than 1 fs. However, we did not find discernable differences in the reaction path presumably because H atoms do not participate actively in the surface reactions. After this, the simulations were continued within the constant number of particles, volume, and energy (NVE) ensemble for another 13 ps. To describe the odd number of electrons in the systems having one Al atom we used the local spin density approximation (Gunnarsson and Lundqvist 1976). Trajectories were animated using the OVITO software package (Stukowski 2010) for analyzing output data.

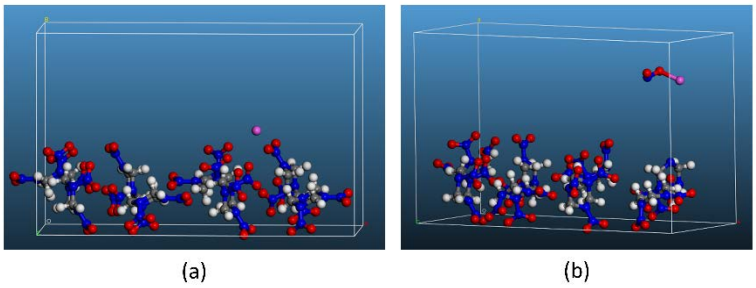

Fig. 26 Simulation unit cell and atom of Al on the [210] surface of RDX. a) Initial position of the Al atom near NO_2 and b) Al-O-N-O molecule departed from the surface after 5.3 ps.

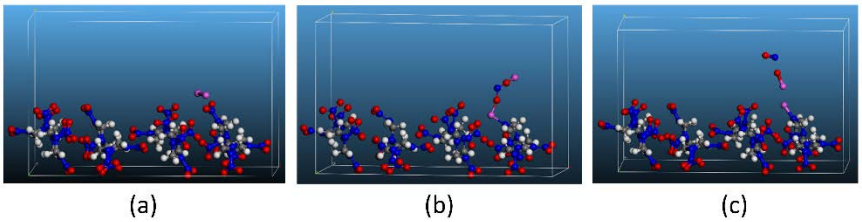

Fig. 27 Simulation unit cell for Al dimer on the [210] surfaces of RDX. a) Initial position of Al dimer, b) formation of the Al-O-N-O-Al-N-$CH_6N_4O_4$ complex at the surface, and c) decomposition of the complex and departing diatomic molecules from the surface.

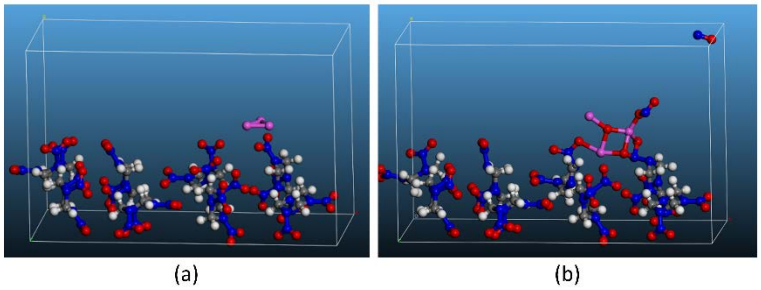

Fig. 28 Al trimer on the surface [210] of RDX. Initial position near NO_2 group of the surface, a) Al complex at the surface, and b) NO molecule removed from RDX after 15 ps.

5.2 Single Al Atom at the RDX Surface

We placed an unpassivated Al atom at various parts of the RDX surface model far and close to the uppermost NO_2 groups of the "rough" [210] surface. In all cases the Al atom moves to the O atoms at the surface NO_2 groups and forms a complex Al-O-N-O- at the surface of RDX: this is a barrierless process. Then Al-O-N-O molecule dissociates and moves away from the surface (Fig. 26b). The Al-O BL in the molecule is 1.992 Å after 5.3 ps.

After removal of the NO_2 group from the surface, the C-N-C angle of the remaining surface fragment changes from 115.120° to 113.486° and the N atom relaxes outwards by 0.2 Å. The Al-O-N-O molecule persists as shown in Fig. 26b after 15

ps; however, this moiety might decompose to Al monoxide and nitric oxide molecules during longer times or/and higher temperatures than that of the current simulation.

5.3 Al Dimer at the RDX Surface

The same type of DFT MD calculations were performed for an Al dimer located near various parts of the RDX surface. The most noticeable changes were observed near the NO_2 groups above the RDX [210] surface (Fig. 27a). After 1 ps of NVT simulations at 100 °C, the formation of the Al-O-N-O-Al-N-CH_6NO complex was observed (Fig. 27b). The Al atom inserted between the surface N atom and O atom of the departing NO_2 group results in the relaxation of the N atom into the surface, and a decrease of the C-N-C angle from 115.129° to 108.859° because of the reduction of the distance between the C atoms by 0.22 Å. A further transformation of the complex to Al monoxide and nitric oxide (Fig. 27c) occurs after NVE simulation with temperature equilibrated around 95 °C.

After decomposition of the complex, the Al-N BL at the surface changes from 1.87 to 1.94 Å and the N atom bonded to Al relaxes outwards by 0.1 Å compared with the initial surface structure of RDX. The BLs of the Al monoxide and nitric oxide molecules are 1.837 and 1.189 Å, respectively, is in reasonable agreement with experimental data (1.844 Å for Al-O [Coheur and Rosen 1941] and 1.151 Å for nitric acid [Brown et al. 1972]).

5.4 Al Trimer at the RDX Surface

We placed an Al trimer at the RDX surface at different places on the RDX surface. The most substantial changes were found for locating the Al trimer near the NO_2 groups as depicted in Fig. 28. The Al trimer dissociates at the surface, Al atoms move away from each other and form complexes at the surface, accompanied by the elimination of a nitric oxide molecule from the surface. The Al trimer decomposes as it approaches the surface, while simultaneously bonding with O atoms on different NO_2 group on surface molecules. Two of the Al atoms each formed the surface complexes Al-O-N-O- (as in single atom case described previously) and departed (similar to Fig. 26b) from the surface of RDX after 3 ps. After 7 ps one of those molecules decomposed into Al-O and N-O molecules. This Al-O molecule and the remaining Al-O-N-O molecules moved back to the surface and after 11 ps complexed with the remaining third Al after 15 ps in Fig. 28b. The passivated Al atoms of the complex have BLs in the range of 1.840 to 2.023 Å. Clearly the surface chemistry involving small Al fragments is quite complex.

The Al-O bond parallel to the surface (upper side of the Al-O square in Fig. 28b) has a length of 1.840 Å, which is surprisingly close to the BL of Al monoxide molecule (Coheur and Rosen 1941). The BL of nitric oxide molecule (1.219 Å) is slightly bigger than that for dimer case (Fig. 27c) and probably indicates a need to use more vacuum space above the surface (than 14 Å) for simulations of the trimer.

6. Conclusions

This report describes experimental and computational modeling efforts exploring the possibility of utilizing nanoscale Al in energetic formulations. The initial experimental focus of the project was changed when challenges involved in synthesizing gas generator passivated Al nanoclusters (i.e., Al_{77} and ligands) proved insurmountable. Instead, by measuring the spatially and temporally resolved temperatures of reacting nano-Al formulations, we were able to demonstrate the need to refine the initial hypothesis for mesoparticle heating put forth in (Wang et al. 2013), since diffusion of atmospheric O_2 through the NC coating does not occur until much later times. All 3 types of laser ignition experiments demonstrated differences in the 2 different batches of mesoparticle samples, which could be explained by differences in the Al nanoparticle source and/or process control issues with the electrospray method. The origin of the observed energy release differences between the 2 batches of samples must be understood before additional conclusions are drawn from this experimental work; however, the preliminary results show a promising enhancement in energy release and combustion efficiency for the mesoparticle samples.

The MD simulations presented in this report indicate that the initial hypothesis of pure nanoscale Al ejection from a gas generator mesoparticle may not be easily achievable. These simulations also lay the groundwork for future MD simulations of passivated nanoclusters, either individually or constructed into a larger mesoparticle. There are many avenues to pursue in future research endeavors, including simulations of larger mesoparticles, different gas generators, varying the rate of temperature increase, and the final temperature. In fact, as part of this work, larger mesoparticles consisting of 400,000 atoms were generated (with both random and uniform distributions of Al_{50} nanoclusters). However, errors associated with balancing the load on multiple processors prevented us from obtaining any results from these systems.

Perhaps the most important results of the section on DFT simulations of Al clusters with energetic materials are that 1) we optimized an Al_{77} structure passivated by high N, high-energy-content ligands and found a need for more complete passivation of subsurface atoms of Al_{77} and Al_{50} clusters by small molecules, 2)

using DFT MD simulations we observed active interaction of unpassivated Al atoms with [210] surface of RDX, mainly with O atoms of NO_2 groups of the surface, including very complex chemical reaction. Such calculations provide insight into the fate of Al atoms and small fragments that might be emitted upon the heating and decomposition of Al nanoclusters passivated with high-energy-content ligands.

There is also the possibility that Al nanoclusters could be passivated by conventional CHNO energetic materials. Formation of Al-O bonds was found in simulations of FOX-7 adsorbed on the surface of Al [111] (Sorescu et al. 2005). The possibility of Al nanocluster passivation by RDX was mentioned in Umezawa et al. (2007) on the basis of DFT simulation of chemisorption of RDX molecule on Al [111] surface. We also found passivation of Al atoms, dimers at the RDX via formation of Al complexes Al-O-N-O…at the surface but only for a short period of time (~1–2 ps). The Al trimer at the surface of RDX forms a complex found to be stable and partly passivated at least for the time of our simulation (15 ps). The lifetime of the Al complex at the surface is gradually increasing from single atom (1 ps) to dimer (2 ps) and to trimer (>15 ps). The trend indicates that bigger and partly passivated nanoclusters of Al might behave less chemically active than Al atoms at the [210] surface of RDX.

7. References

Akbarzadeh H, Shamkhali AN, Abbaspour M, Salemi S. Molecular dynamics investigation of the deliquescence of NH_4Cl and NH_4NO_3 nanoparticles under atmospheric conditions. RSC Adv. 2015;5(48):38345–38353.

Alavi S, Velardez GF, Thompson DL. Molecular dynamics studies of nanoparticles of energetic materials. MRS Proceedings. 2003;800:AA8.5

Bodnarchuk MS, Heyes DM, Breakspear A, Chahine S, Dini D. A molecular dynamics study of $CaCO_3$ nanoparticles in a hydrophobic solvent with a stearate co-surfactant. Phys Chem Chem Phys. 2015;17(20):13575–13581.

Brousseau P, Anderson CJ. Nanometric aluminum in explosives. Propellants Explos Pyrotech. 2002;27(5):300–306.

Brown JM, Cole ARH, Honey FR. Magnetic dipole transitions in the far infra-red spectrum of nitric oxide. Mol Phys. 1972;23(2):287–295.

Coheur FP, Rosen B. Le spectre de bandes de l'oxyde d'aluminium. Bull Soc R Sci Liege. 1941;10:405–413.

Ding L, Davidchack RL, Pan J. A molecular dynamics study of sintering between nanoparticles. Comp Mat Sci. 2009;45(2):247–256.

Dlott DD. Thinking big (and small) about energetic materials. Mater Sci Technol. 2006;22(4):463–473.

Evteev AV, Levchenko EV, Riley DP, Beloca IV, Murch GE. Reaction of a Ni-coated Al nanoparticle to form *B2*-NiAl: a molecular dynamics study. Phil Mag Lett. 2009;89(12):815–830.

Fujihisa H, Honda K, Obata S, Yamawaki H, Takeya S, Gotoh Y, Matsunaga T. Crystal structure of anhydrous 5-aminotetrazole and its high-pressure behavior. Cryst Eng Comm. 2011;13(1):99–102.

Goedecker S, Teter M, Hutter J. Separable dual-space Gaussian pseudopotentials. Phys Rev B. 1996;54(3):1703–1710.

Gottfried JL. Laser-induced plasma chemistry of the explosive RDX with various metallic nanoparticles. Appl Optics. 2012;51(7):B13–B21.

Gottfried JL. Influence of exothermic chemical reactions on laser-induced shock waves. Phys Chem Chem Phys. 2014;16(39):21452–21466.

Gottfried JL, Munson CA, Colburn J, Beyer RA. Initial testing of a prototype laser ignition chamber. Aberdeen Proving Ground (MD): Army Research Laboratory (US); 2014 Mar. Report No.: ARL-TR-6862.

Gunnarsson O, Lundqvist BI. Exchange and correlation in atoms, molecules, and solids by the spin-density-functional formalism. Phys Rev B. 1976;13(10):4274–4298.

Hattemer GD, Arya G. Viscoelastic properties of polymer-grafted nanoparticle composites from molecular dynamics simulations. Macromolecules. 2015;48(4):1240–1255.

Henz eBJ, Hawa T, Zachariah M. Molecular dynamics simulation of the energetic reaction between Ni and Al nanoparticles. J Appl Phys. 2009;105(12):124310.

Hong S, van Duin ACT, Molecular dynamics simulations of the oxidation of aluminum nanoparticles using the ReaxFF reactive force field. J Phys Chem C. 2015;119(31):17876–17886.

Hutter J, Iannuzzi M, Schiffmann F, VandeVondele J. CP2K: atomistic simulations of condensed matter systems. WIREs Comput Mol Sci. 2014;4(1):15–25.

Kaur K. Prakash S, Goyal N, Singh R, Entel P. Structure factor of amorphous TiO_2 nanoparticle; molecular dynamics study. J Non-Cryst Solids. 2011;357(19):3399–3404.

Klapotke TM, Piercey DG, Stierstorfer J. Amination of energetic anions: high-performing energetic materials. Dalton Trans. 2012;41(31):9451–9459.

Knorowski C, Burleigh S, Travesset A. Dynamics and statics of DNA-programmable nanoparticle self-assembly and crystallization. Phys Rev Lett. 2011;106(21):215501.

Larentzos JP, Rice BM, Byrd EFC, Weingarten NS, Lill JV. Parameterizing complex reactive force fields using multiple objective evolutionary strategies (MOES). Part 1: ReaxFF models for cyclotrimethylene trinitramine (RDX) and 1,1-diamino-2,2-dinitroethene (FOX-7). J Chem Theory Comput. 2015;11(2):381–391.

Lesnikovich AI, Ivashkevich OA, Levchik SV, Balabanovich AI, Gaponik PN, Kulak AA. Thermal decomposition of aminotetrazoles. Themochim Acta. 2002;388(1):233–251.

Liu L, Liu Y, Zybin SV, Sun H, Goddard WA. ReaxFF-lg: correction of the ReaxFF reactive force field for London dispersion, with applications to the equations of state for energetic materials. J Phys Chem A. 2011;115(40):11016–11022.

Paul KW, Hurley MM, Irikura KK. Unimolecular decomposition of 5-aminotetrazole and its tautomer 5-iminotetrazole: new insight from isopotential searching. J Phys Chem A. 2009;113(11):2483–2490.

Perdew JP, Burke K, Ernzerhof M. Generalized gradient approximation made simple. Phys Rev Lett. 1996;77(18):3865–3868.

Perdew JP, Chevary JA, Vosko SH, Jackson KA, Pederson MR, Singh DJ, Fiolhais C. Atoms, molecules, solids, and surfaces: applications of the generalized gradient approximation for exchange and correlation. Phys Rev B. 1992;46(11):6671–6687.

Plimpton S. Fast parallel algorithms for short-range molecular dynamics. J Comp Phys. 1995;117(1):1–19.

Politzer P, Lane P, Grice ME. Energetics of aluminum combustion. J Phys Chem A. 2001;105(31):7473–7480.

Rice BM, Larentzos JP, Byrd FC, Weingarten NS. Parameterizing complex reactive force fields using multiple objective evolutionary strategies (MOES): Part 2: transferability of ReaxFF models to C-H-N-O energetic materials. J Chem Theory Comput. 2015;11(2):392–405.

Sang LV, Hoang VV, Hang NTT. Molecular dynamics simulation of melting of fcc Lennard-Jones nanoparticles. Eur Phys J D. 2013;67:64.

Segall MD, Lindan PJD, Probert MJ, Pickard CJ, Hasnip PJ, Clark SJ, Payne MC. First-principles simulation: ideas, illustrations and the CASTEP code. J of Phys Condens Matter. 2002;14(11):2717–2744.

Sen FG, Qi Y, van Duin ACT, Alpas AT. Oxidation induced softening in Al nanowires. Appl Phys Lett. 2013;102(5):051912.

Shen T, Meng W, Wu Y, Lu X. Size dependence and phase transition during melting of fcc-Fe nanoparticles: a molecular dynamics simulation. Appl Surf Sci. 2013;277:7–14.

Sorescu DC, Boatz JA, Thompson DL. First-principles calculations of the adsorption of nitromethane and 1,1-diamino-2,2-dinitroethylene (FOX-7) molecules on the α-Al_2O_3 (0001) surface. J Phys Chem B. 2005;109(4):1451–1463.

Stukowski A. Visualization and analysis of atomistic simulation data with OVITO–the open visualization tool. Model Simul Mater Sci. 2010;18(1):015012.

ter Horst JH, Geertman RM, van der Heijden AE, van Rosmalen GM. The influence of a solvent on the crystal morphology of RDX. J Cryst Growth 1999;198/199:773–779.

Umezawa N, Kalia RK, Nakano A, Vashista P, Shimojo F. 1,3,5-trinitro-1,3,5-triazine decomposition and chemisorption on Al(111) surface: first principles molecular dynamics study. J Chem Phys. 2007;126(23):234702.

van Duin ACT, Dasgupta S, Lorant F, Goddard WA. ReaxFF: a reactive force field for hydrocarbons. J Phys Chem A. 2001;105(41):9396–9409.

Vollet J, Hartig JR, Schnöckel H. $Al_{50}C_{120}H_{180}$: a pseudofullerene shell of 60 carbon atoms and 60 methyl groups protecting a cluster core of 50 aluminum atoms. Ang Chem. 2004;43(24):3186–3189.

Wang H, Jian G, Egan GC, Zachariah MR. Assembly and reactive properties of Al/CuO based nanothermite microparticles. Combust Flame. 2014;161(8):2203–2208.

Wang H, Jian G, Yan S, DeLisio JB, Huang C, Zachariah MR. Electrospray formation of gelled nano-aluminum microspheres with superior reactivity. ACS Appl Mater Interfaces. 2013;5(15):6797–6801.

Williams GK, Palopoli SF, Brill TB. Thermal decomposition of energetic materials. Combustion and Flame. 1994;98(3):197–204.

Williams KS, Hooper JP. Structure, thermodynamics, and energy content of aluminum-cyclopentadienyl clusters. J Phys Chem A. 2011;115(48):14100–14109.

Zeng Q, Jiang X, Yu A, Lu G. Growth mechanisms of silver nanoparticles: a molecular dynamics study. Nanotechnology. 2007;18(3):035708.

List of Symbols, Abbreviations, and Acronyms

5-ATZ	5-aminotetrazole
Al	aluminum
CSP	conventional spray pyrolysis
CuO	copper oxide
DFT	density functional theory
DSC	differential scanning calorimetry
EDS	energy dispersive spectroscopy
ES	electrosprayed
GGA	generalized gradient approximation
H	hydrogen
IR	infrared
LAMMPS	Large-scale Atomic/Molecular Massively Parallel Simulator
MD	molecular dynamics
N	nitrogen
NC	nitrocellulose
np	nanoparticles
NPT	isothermal-isobaric ensemble
NVE	microcanonical ensemble
NVT	canonical ensemble
NsT	isothermal-isostress ensemble
O	oxygen
PM	physically mixed
POM	polyoxometallate
RDX	cyclotrimethylene trinitramine
SEM	scanning electron microscopy

SiO_2	silica
TEM	transmission electron microscopy
TGA	thermogravimetric analysis
TZ	tetrazole

1 (PDF)	DEFENSE TECHNICAL INFORMATION CTR DTIC OCA
2 (PDF)	DIRECTOR US ARMY RESEARCH LAB RDRL CIO LL IMAL HRA MAIL & RECORDS MGMT
1 (PDF)	GOVT PRINTG OFC A MALHOTRA
14 (PDF)	DIR USARL RDRL WML B N WEINGARTEN J GOTTFRIED I BATYREV E COLLINS J BRENNAN E BYRD S IZVYEKOV W MATTSON B RICE D TAYLOR N TRIVEDI J LARENTZOS R SAUSA R PESCE-RODRIGUEZ
1 (PDF)	RDRL WML M ZOLTOSKI

INTENTIONALLY LEFT BLANK